ONE-DIMENSIONAL RESPONSE OF A BOREHOLE STATION DURING THE 2005 WEST OFF FUKUOKA PREFECTURE EARTHQUAKE: OBSERVATION AND SIMUALTION

F. De Martin[1], H. Kawase[2] and A. Modaressi[3]

[1] *Engineer, Development Planning and Naturals Risks Division, brgm, Orléans. France*
[2] *Professor, Disaster Management for Safe and Secure Society, Disaster Prevention Research Institute, Kyoto, Japan*
[3] *Professor, Laboratoire Mécanique des Sols, Structures et Matériaux CNRS UMR 8579, Ecole Centrale de Paris, Chatenay-Malabry, France*
Email: f.demartin@brgm.fr, kawase@zeisei.dpri.kyoto-u.ac.jp, arezou.modaressi@ecp.fr

ABSTRACT :

The objective of this paper is to present a one-dimensional response of a soil column at a borehole station during the 2005 west off Fukuoka prefecture, Japan, earthquake. The borehole station is located in Fukuoka City where the sediment's thickness reaches 56 meters. First, we have confirmed that according to the rupture process the major axis is north 32 degrees east by calculating the observed energy distribution at several stations around the epicenter. Then we have computed, in the major and minor axes, surface-to-borehole spectral ratios using the S-wave portion of the main shock and 12 aftershocks. As for the aftershocks, the fundamental resonant peaks lie in the frequency range of 1.5 to 1.9 Hz, and are quite stable. As for the main shock, the resonant peak is 1.3 Hz showing a nonlinear effect. To simulate the main shock, we have first inverted by genetic algorithm S-waves velocities and damping coefficients of the soil column as well as incident angle of the upcoming wave using Thomson-Haskell propagator matrix for SH and P-SV waves. Inverted values of S-waves velocities are consistent with the P-S logging provided by CTI Engineering and inverted incident angle is also consistent with observed particle orbit in the vertical plane. Simulations at the borehole station show a good agreement with observations.

KEYWORDS: borehole observation simulation propagator inversion genetic-algorithm

1. INTRODUCTION

It is now recognized that the ground motions observed at two sites, even within a short distance, are different from each other because of site effects due to local geology. Hence, the importance of local site geology in seismic design is nowadays well established and the evaluation of site effects on strong ground motion has been extensively studied during the last three decades and is thoroughly reviewed (e.g., Aki [1988]).

In order to understand site effects, the one-dimensional (1-D) modeling of soil amplification has been proved to be a good approximation for most cases. In recent years, 2-D or 3-D effects of basins are found to be relevant for several cases of strong ground motion (e.g., Kawase and Sato [1992]). However, those effects are essentially predominant in the low-frequency range ($\leq$ 1Hz) and since seismic waves with shorter wavelength are more vulnerable to mutual interference of multiple reflection/refraction and to intrinsic/scattering attenuation, 2-D or 3-D effects in higher frequency would easily disappear. Moreover, it has been shown during two blind-prediction experiments conducted by the IASPEI/IAEE Joint Working Group on Effects of Surface Geology on Strong Motions (e.g., Midorikawa [1992]) that precision of the geological structure is more important than the model dimension. Therefore, we study in this paper the 1-D response of a borehole station by focusing on the geological structure. 2-D or 3-D effects could be taken into account for further study.

After the 2005 west off Fukuoka earthquake, different studies have been pursued on Fukuoka City basin. Simulations of strong motions within the entire basin using 1-D theory showed that the largest PGV (about 80

cm/s) was located in the northeast side of the Kego fault where the Quaternary sediments are the deepest (e.g., Satoh and Kawase [2006]).

In this study, we first demonstrate that the major axis of the main shock within Fukuoka City basin is approximately the fault perpendicular direction (≈N32°E) by calculating the observed energy distribution at 22 stations within 60 km from the epicenter. Then we compute, in the major and minor axes, observed surface-to-borehole spectral ratios at CTI borehole station using the S-wave portion of the main shock and 12 aftershocks. Then, to simulate the main shock, we invert by genetic algorithm S-waves velocities and damping coefficients of the soil column as well as incident angle of the upcoming wave using Thomson-Haskell propagator matrix method for SH and P-SV waves (e.g., Thomson [1950], Haskell [1953]).

2. OBSERVATION

2.1 Overview of the Strong Ground Motion

Fukuoka City is located on the northern part of Kyushu Island, southwestern part of Japan (Figure 1 left panel). The 2005 west off Fukuoka prefecture earthquake with JMA (Japanese Meteorological Agency) magnitude MJ of 7.0 (Mw = 6.6) and focal depth of 9.2 km occurred on 20 March 2005 in the north coast of Kyushu Island within the prolongation of the Kego fault. Figure 1 right panel shows the Kego fault (solid line at the southwestern side of the station FKO006) and accelerograms at some stations surrounding the epicenter. We can see at a glance that the accelerogram at FKO006 exhibits longer vibration periods than other stations. This observation is consistent with the geology at station FKO006 composed of Quaternary sediments of around 30 meters depth. Other stations situated on engineering bedrock show accelerograms with shorter periods.

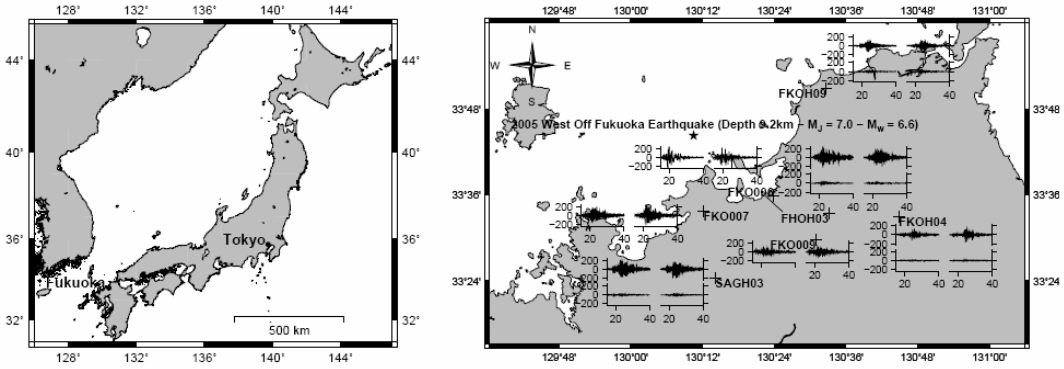

Figure 1: Left panel: localization of Fukuoka City, northern part of Kyushu Island, Japan. Right Panel: location of the Kego fault (solid line at the south-western side of the station FKO006) and accelerograms recorded at stations surrounding the epicenter (pointed out by a star) of the Fukuoka earthquake.

2.2 Energy Distribution and Theoretical Radiation Pattern

We first confirm the major and minor axes using the energy distribution in the horizontal plane at 22 stations. The energy distribution, given by Takizawa [1982] and successfully used to confirm major axis of strong motion by Kawase and Aki [1990], consist of calculating the total power and cross spectra of the two orthogonal components n (referring to north) and e (referring to east) in the frequency range of interest:

$$[E] = \int_{\omega 1}^{\omega 2} \Re \begin{pmatrix} S_{nn}(\omega) & S_{ne}(\omega) \\ S_{en}(\omega) & S_{ee}(\omega) \end{pmatrix} d\omega,$$

where Snn(ω) is a velocity power spectrum of the n direction and Sne(ω) is a velocity cross power spectrum between the n and e direction, and so on. Then, the energy in the direction Φ measured clockwise from the n-axis can be obtained as

$$E_\phi = \{\cos\phi, \sin\phi\}[E]\left\{\begin{array}{c}\cos\phi\\ \sin\phi\end{array}\right\}.$$

This energy distribution will be two elliptic lobes in line with the major axis if the ground motion is unidirectional, while it will become a single circle if the ground motion is not directional at all.

Fukuoka earthquake being a strike-slip crustal earthquake with a strike direction equal to N122°E, a dip angle of 89° and a rake angle of -11° (e.g., Asano and Iwata [2006]) we can first plot theoretical far-field radiation pattern of the so-called Double Couple mechanism in an infinite homogeneous medium to have in mind predominant direction of motion. Figure 2 shows radiation pattern for P- and S-waves and for SH and SV components. The fault plane and the auxiliary plane are nodal lines for P-wave whereas they are predominant plane for S-wave. By decomposition of S-wave into SH and SV component, we see that SH component is predominant in the fault plane and in the auxiliary plane whereas these planes are nodal lines for SV component.

Figure 3 shows the energy distribution calculated in the horizontal plane for records observed at 22 stations (it should be noted that if necessary, energy distributions have been corrected by rotation of sensors). Depending on stations, the observation shows more or less a good agreement with the solution of the double couple point source model. The energy distribution in the fault plane at the stations FKOS02, FKOS05, FKOS06 and FKO009 shows a good coherence since it exhibits a major axis perpendicular to the fault plane (i.e., predominance of SH-component). The same agreement can be seen for the auxiliary plane, where stations SAG001, SAGH01 and FKOH09 exhibit the same predominance. However, within Fukuoka City, we can notice that the energy distribution of FKO006, FKOS01 and CTI is slightly rotated toward north. This rotation could be due to an arrival of later phases (e.g., trapped waves (Li and Leary [1990])) after the main train of S-wave.

2.3 Surface-to-Downhole Spectral Ratios

Records of the borehole station with a sample frequency of 100 Hz have been provided by CTI Engineering Co., Ltd which is located where the thickness of sediment reaches 56 meters. Two sensors are situated below their base-isolated building, one at the free surface and the other one at 65 meters below the free surface embedded in the bedrock. As the building is base-isolated, soil-structure interaction has been neglected and the surface ground motion has been considered as a free field ground motion. A section cut realized at 210 meters on the northern part of the borehole station is shown in Figure 4 left panel (Geological Survey Association of Kyushu, Fukuoka soil map [1981]). The associated 1-D velocity profile is shown in Figure 4 right panel. The top 17 meters mainly consists of sand (Arae formation) whose S-wave velocity increases from 150 m/s to 361 m/s, and then 8 meters of clay are present whose S-wave velocity is around 230 m/s. Then follow thin layers of sand and clay and 13 meters of sand (Hakata formation), whose S-wave velocity ranges between 292 m/s and 495 m/s. Below, the engineering bedrock is made of mudstone dating from the pre-Tertiary period of Cenozoic era whose S-wave velocity has been supposed as 650m/s. For computation of spectral ratios, the following procedure has been used:

- accelerograms have been band-pass filtered in the frequency range [0.1-10] Hz with a 6th order Butterworth filter;
- a cosine shape of 25% of the time window has been applied at both ends of the selected S-wave portion;
- to compute the Fast Fourier Transformation, a number of data samples N equal to 4,096 has been chosen to have a fine frequency resolution;
- Fourier spectra have been smoothed with a spectral Parzen bandwidth of 0.4 Hz in order to remove non-physical peaks.

Figure 5 exposes spectral ratios computed for the main shock and the aftershocks in fault perpendicular and fault parallel directions.

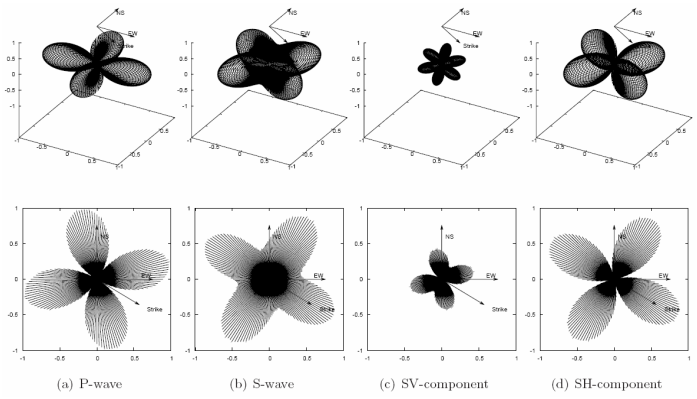

Figure 2 : Theoretical radiation pattern of far-field wave for a double couple point source model in an infinite homogeneous medium oriented as followed: strike = 122°, dip = 87° and rake = -11°. Panels (a) and (b) show P- and S-wave radiation pattern, respectively. Panels (c) and (d) expose SV and SH component of the S-wave, respectively. Top panels show a 3-D view of the radiation patterns and bottom panels show them mapped into the horizontal plane. The panel (d) clearly exposes a predominance of the SH-component in the fault plane and in the auxiliary plane.

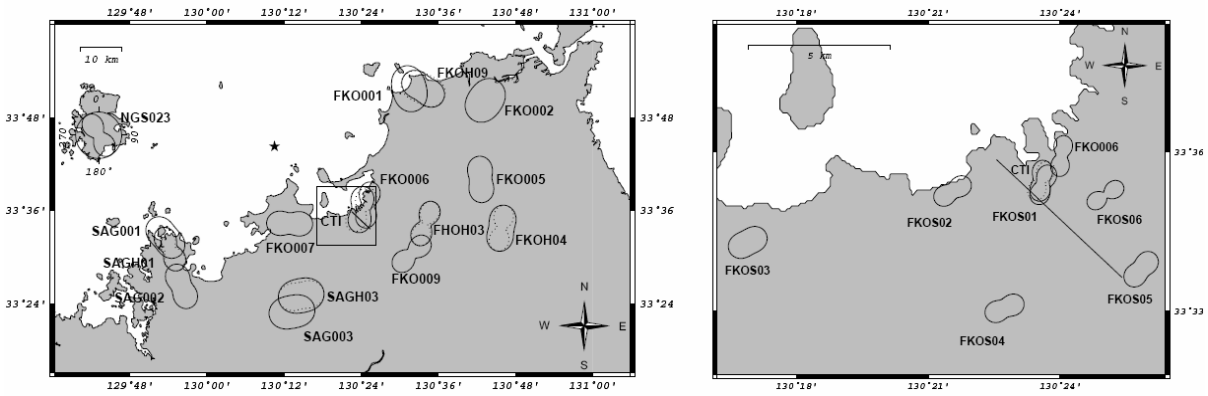

Figure 3: Energy distribution in the horizontal plane (NS-EW) for the records observed at 22 stations within 60 km from the epicenter. The principal axis measured clockwise from the north (see station NGS023) has +/- 180° ambiguity. The energy distribution is calculated from velocity power spectra which are derived from NS and EW components of velocity seismograms (the entire record has been used to compute the power spectra). The frequency range used to integrate a power spectrum is 0.1 to 10 Hz. Solid lines represent the energy distribution calculated at the free surface sensor and dash lines that of the downhole sensor. The rectangle on the left-hand side panel denotes the area shown on the right-hand side panel. The approximate location of the Kego fault is represented by a solid straight line (both panels) and the epicenter of the earthquake by a star (left panel only).

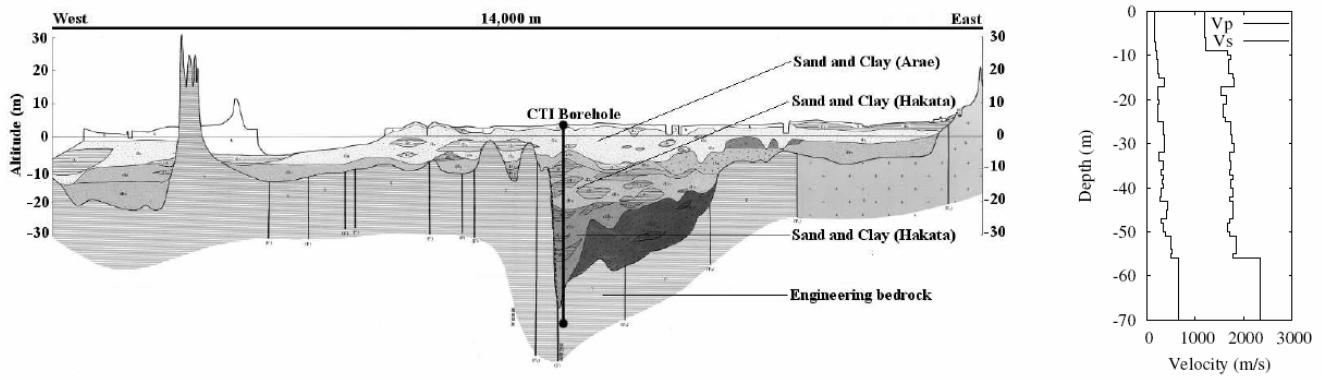

Figure 4: Left panel: east-west section cut located at 210 meters on the northern part of CTI borehole station. The vertical axis has been exaggerated. The borehole station is indicated by a solid line and the sensors are represented by two points along this line. The upper sensor is located at the free surface, below the base isolation and the downhole sensor is embedded in the bedrock. Right panel: 1-D velocity profile along the borehole station provided by CTI Engineering Co., Ltd.

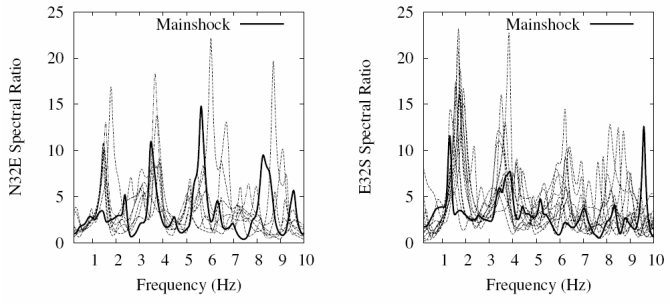

Figure 5: Spectral ratios computed at CTI borehole station (left-panel: fault perpendicular direction; right-panel: fault parallel direction). The spectral ratio of the main shock is plotted with a thick line.

For the aftershocks, whose PGAs range from 2 cm/s^2 to 32 cm/s^2, we notice that spectral ratios exhibit a fundamental mode around 1.5 Hz and 1.9 Hz. The second mode is present around 3.7 Hz. Other higher modes are present around 6.0 Hz and 8.5 Hz. During the main shock, the fundamental mode is not clearly visible on the fault perpendicular direction. However, it is clear on the fault parallel direction and its frequency is around 1.3 Hz. Higher modes are visible for the fault perpendicular direction but not so much for the fault parallel direction.

The shift of frequency from 1.9 Hz during aftershocks to 1.3 Hz during the main shock suggests a nonlinear behavior of the soil. This nonlinear behavior can be seen by calculating the cross-correlation between the downhole and surface sensors (e.g., Kawase and Sato [1992]). Figure 6 left panel exposes the time delay against the PGA. As the PGA increases, the time delay increases as well; this denotes a decrease of the S-wave velocity and thus points out a nonlinear effect. Middle and right panel show an example of cross-correlation calculated for the main shock and for an aftershock. The positive peak between 0 and -0.5 second denotes the time delay of the S-wave recorded at the free surface sensor with respect to the S-wave recorded at the downhole sensor. A larger time delay is seen for the main shock.

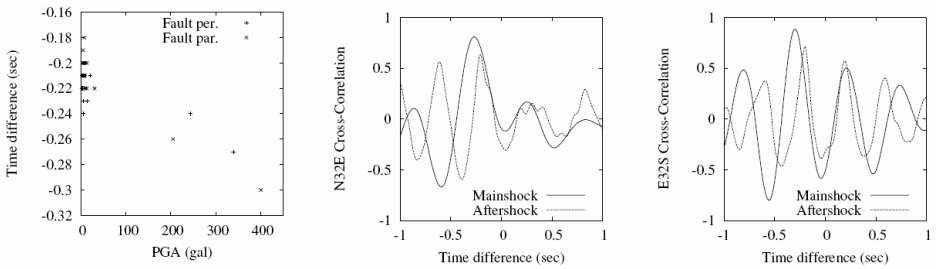

Figure 6: Left panel: Time delay plotted against PGA. Middle and right panel: Example of cross correlation computed on the S-wave part of the main shock and of an aftershock.

3. SIMULATION

3.1 Inversion of S-wave Velocities and Damping Coefficients Considering Obliquely Incident Wave

Before simulating the main shock, we have inverted by genetic algorithm (e.g., Goldberg [1989]) S-wave velocities (Vs) and damping factors of the soil column as well as incident angle of the upcoming wave using Thomson-Haskell propagator matrix for SH and P-SV waves. The original P-S logging from CTI has been divided into 5 parts by taking into account S-wave velocity similarity (on 56 meters of sediment, 43 have been inverted to limit number of parameters to invert). Each part is affected by coefficients to be optimized for S-wave velocities and damping factors. Initial values for S-wave velocities are those from P-S logging. Coefficients to optimize were constrained in the range [0.5-1.2] with a discretization of 0.0055 (1.0 being P-S logging values). Damping factor has been chosen of the form $h_0 f^{-\alpha}$, with f the frequency (e.g., Satoh et al. [2001]). Initial values are 0.05 for h_0 and 0.4 for α. The interval for h_0 and α is [0.3-2.5] with a discretization of 0.07 and incident angle precision is 0.96°. A general scheme of the optimization by genetic algorithm is show in Figure 7 left panel. The initial population step generates N individuals representing coefficients to be optimized

in binary format (information contained in one individual represent the first 43 meters of the soil column plus the incidence angle). Then, during the evaluation step, theoretical spectral ratios are computed for each individual and the objective function for an individual is computed by the following formulae:

$$E(\mathbf{x}) = \frac{1}{2}\left[\frac{\int_{f_s^{SH}}^{f_e^{SH}} |H_{SH}^0(f) - H_{SH}(f,\mathbf{x})|^2 df}{\int_{f_s^{SH}}^{f_e^{SH}} |H_{SH}^0(f)|^2 df} + \frac{\int_{f_s^{PSV}}^{f_e^{PSV}} |H_{PSV}^0(f) - H_{PSV}(f,\mathbf{x})|^2 df}{\int_{f_s^{PSV}}^{f_e^{PSV}} |H_{PSV}^0(f)|^2 df}\right]$$

where H^0_{SH} and H^0_{PSV} are observed fault perpendicular and fault parallel surface-to-borehole spectral ratios represented theoretically by H_{SH} (the ratio of SH-waves at the free surface to the obliquely incident SH-waves at the bedrock) and H_{PSV} (the ratio of the horizontal components of SV-waves and P-waves at the free surface to the horizontal component of SV-waves at the bedrock) as assumed by Satoh [2006]. **x** is the vector to be optimized and f_e^{SH}, f_s^{SH}, f_e^{PSV} and f_s^{PSV} the frequency range of integration for SH ratio and PSV ratio respectively. In our study, we have chosen 2.7, 7.4, 0.5 and 5.0, respectively, based on the clarity of predominant peaks.

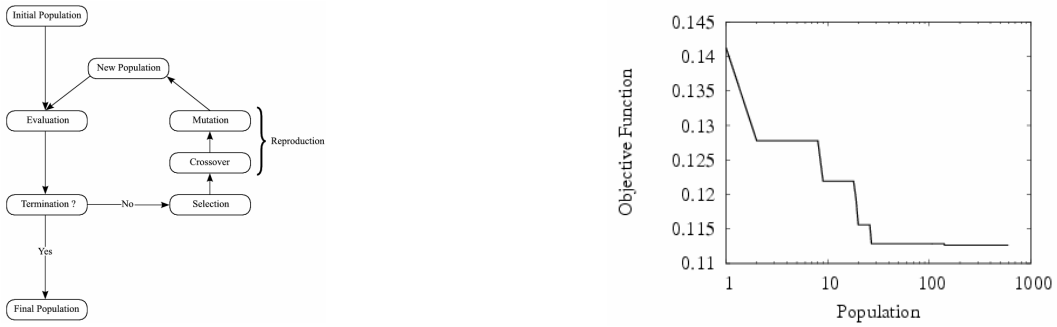

Figure 7: General scheme of optimization by genetic algorithm (left panel). Evolution of objective function with respect to population during the inversion of the soil column of the main shock (right panel).

If the termination criterion is not reached (i.e., small value of E(**x**) or large number of population) then half of the population P is selected by roulette-wheel to constitute parents who give birth to offspring through the crossover step (uniform crossover has been used for the optimization). Finally, very few or no individuals are mutated with a low probability (i.e., one or more of their bytes are changed from 1 to 0 or *vice versa*) to create the new population P+1 and so on. Evolution of the objective function for inversion of the main shock is exposed in Figure 7 right panel; inverted and observed SH and P-SV ratios for the main shock and two inverted and observed P-SV ratios of aftershocks are shown in Figure 8.

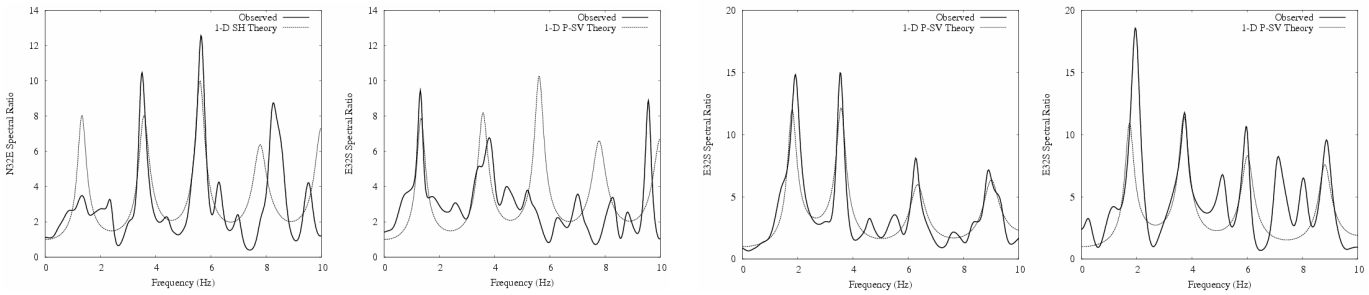

Figure 8: Two left panels: observed and inverted spectral ratios of the main shock for fault perpendicular and fault parallel direction. Two right panels: observed and inverted ratios for two aftershocks for fault parallel direction.

Inverted values of Vs, h_0 and α are plotted together with their initial values in Figure 9. We can see that for the main shock inverted values of Vs are consistent with PS-logging values except around -17 meters and -30 meters where P-S logging shows high local values. Inverted shear wave velocities for the two aftershocks clearly exhibit higher values than for the main shock, showing the evidence of nonlinear behavior of the soil

during the main shock.

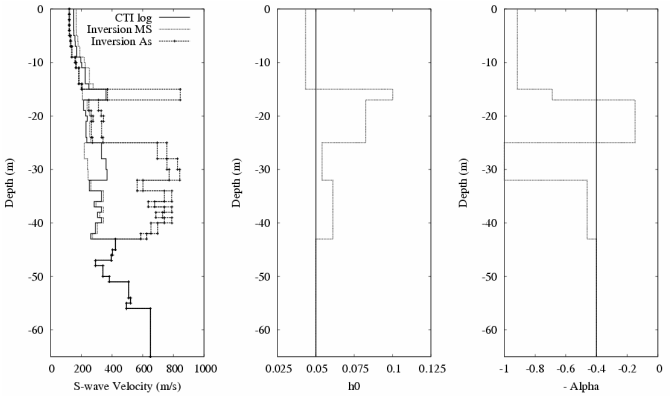

Figure 9: Inverted values of the top 43 meters and initial values of the entire column for Vs (left panel), h0 (middle panel) and -α (right panel). For Vs only, inversions for two aftershocks are plotted as well (lines with points). Around 40 meters depth, the ratio of inverted S-wave velocity for aftershocks to P-S logging velocity is around 220%.

As an example, for the main shock, the inverted incidence angle is 8.7° and is consistent with the particle orbits on a vertical plane calculated from borehole accelerograms as shown in Figure 10.

Figure 10: Particle orbits on a vertical plane calculated from borehole accelerograms at the onset of S-wave portion of the main shock. The orbits are calculated from band-pass filtered waves in the frequency range of interest.

3.2 Simulation of borehole and free surface waveforms

Using inverted SH and P-SV ratios, we have simulated borehole seismograms using free surface records and *vice versa*. Simulations are presented in Figure 11. The downhole simulation in N32°E direction agrees fairly well with observation whereas the E32°S simulation tends to overestimate PGVs. Agreement for free surface simulation is still reasonable; however, PGVs are overestimated for the N32°E direction.

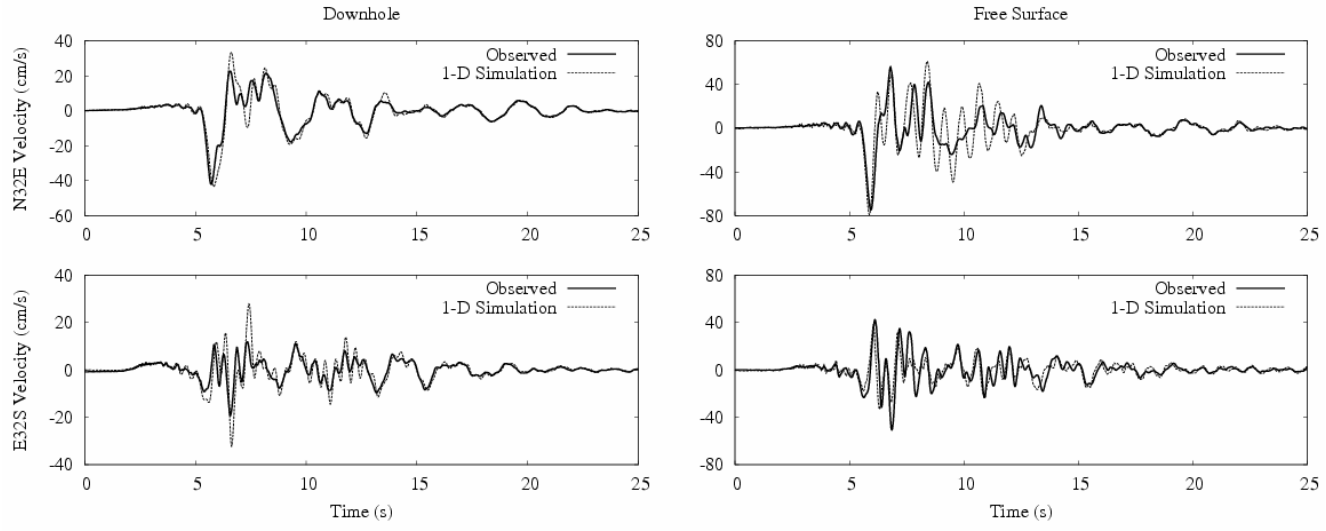

Figure 11: Simulation of borehole seismograms (left panels) and free surface seismograms (right panels).

4. CONCLUSION

We have analyzed the one-dimensional response of CTI borehole station during the 2005 west off Fukuoka prefecture earthquake. We have first found that major and minor axes were N32°E and E32°S, respectively, by computing energy distribution at several stations around the epicenter. Then, thanks to observed surface-to-borehole spectral ratios, we have inverted S-waves velocities, damping factors and incidence angle via Thomson-Haskell propagator matrix method. Simulations have been performed and reasonably reproduced observations; however, further simulations should be done to understand overestimation of PGVs. High values of inverted Vs for the two aftershocks suggest that further inversions should be done on the entire soil column. We would like to express our sincere thanks to CTI Engineering Co. Ltd. for allowing us to analyze their data.

REFERENCES

Aki, K. (1988). Local site effects on strong ground motion. *In Park City, editor, Proc. Earthquake Engineering and Soil Dynamics II GT Div/ASCE*, 103-155.

Geological Survey Association of Kyushu, Fukuoka soil map. (1981). Editing Group of Fukuoka Soil Map.

Goldberg, G.E. (1989). Genetic algorithms in search, optimization, and machine learning. New York, Addison-Wesley.

Haskell, N.A. (1953). The dispersion of surfaces waves in multilayered media. *Bulletin of the Seismological Society of America* **43:**, 17-34.

Kawase, H. and Aki, K. (1990). Topography effect at the critical SV-wave incidence: possible explanation of damage pattern by the Whittier Narrows, California, earthquake of 1 October 1987. *Bulletin of the Seismological Society of America* **80:1**.

Kawase, H. and Sato, T. (1992). Simulation analysis of strong motions in Ashigara valley considering one- and two-dimensional geological structures. *J. Phys. Earth* **40:**, 27-56.

Li, Y.G. and Leary, P.C. (1990). Fault zone trapped seismic waves. *Bulletin of the Seismological Society of America* **80:5**, 1245-2271.

Midorikawa, S. (1992). A statistical analysis of submitted predictions for the Ashigara valley blind prediction test. *In Japan ESG, Odawara, editor, Int. Sym. Effects of Surf. Geol. on Seismic Motion* **II:**, 65-77.

Satoh, T. Fushimi, M. and Tatsumi, Y. (2001). Inversion of strain-dependent nonlinear characteristics of soils using weak and strong motions observed by borehole sites in Japan. *Bulletin of the Seismological Society of America* **91:2**, 365-380.

Satoh, T. (2006). Inversion of Qs of deep sediment form surface-to-borehole spectral ratios considering obliquely incident SH and SV waves. *Bulletin of the Seismological Society of America* **96:3**, 943-956.

Satoh, T. and Kawase, H. (2006). Simulation of strong motions in Fukuoka city during the 2005 west off Fukuoka prefecture earthquake with a special reference to thick quaternary sediments around the Kego fault. *Earth Planets Space* **58:**, 105-110.

Takizawa, H. (1982). Work done by earthquake ground shacking upon various types of dynamics systems. *In Proc. of 6th Japan Earthquake Engineering Symposium*, 1065-1072.

Thomson, W.T. (1950). Transmission of elastic waves through a stratified solid. Journal of Applied Physics **21:**, 89-93.